Flow reversals in a natural circulation loop at atmospheric pressure

S. Renaudière de Vaux, P. Aubert, B. Grosjean, L. Rossi

To cite this version:

S. Renaudière de Vaux, P. Aubert, B. Grosjean, L. Rossi. Flow reversals in a natural circulation loop at atmospheric pressure. International Journal of Heat and Mass Transfer, 2024, 235, pp.126119. ⟨10.1016/j.ijheatmasstransfer.2024.126119⟩. ⟨cea-04695214⟩

HAL Id: cea-04695214

https://cea.hal.science/cea-04695214v1

Submitted on 12 Sep 2024

Graphical Abstract

Flow reversals in a natural circulation loop at atmospheric pressure

S. Renaudière de Vaux, Ph. Aubert, B. Grosjean, L. Rossi

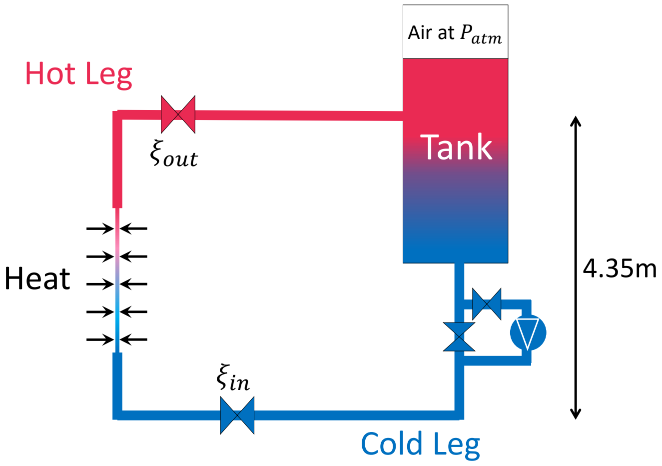

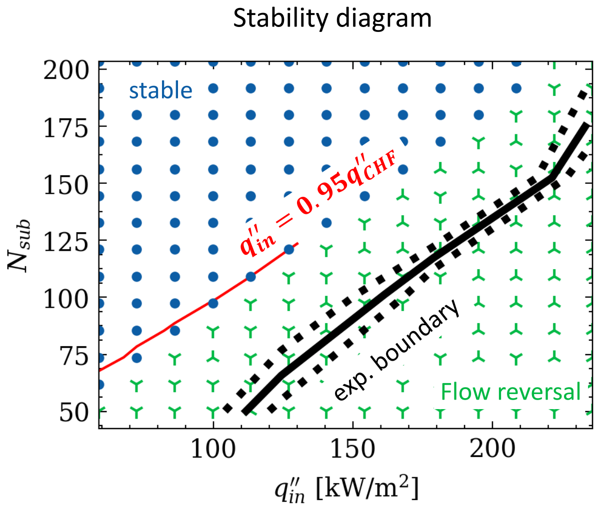

Highlights

Flow reversals in a natural circulation loop at atmospheric pressure

S. Renaudière de Vaux, Ph. Aubert, B. Grosjean, L. Rossi

- The system-scale code CATHARE reproduces satisfactorily the flow reversal regime boundaries;
- At low pressure, the instabilities appear simultaneously with boiling ;
- Increase of upstream (resp. downstream) pressure losses improves (resp. decreases) flow stability.

Flow reversals in a natural circulation loop at atmospheric pressure

S. Renaudière de Vaux[a,*], Ph. Aubert[b], B. Grosjean[a], L. Rossi[b]

[a]*CEA Cadarache (French Atomic Energy Commission), DES/IRESNE/DER,*
Service d'Études des Systèmes Innovants (SESI), 13108 Saint-Paul-lez-Durance, France
[b]*CEA Cadarache (French Atomic Energy Commission), DES/IRESNE/DTN,*
Service de Technologies des Composants et des Procédés (STCP), 13108 Saint-Paul-lez-Durance, France

---

Abstract

Natural circulation in a two-phase water loop with imposed wall power, is investigated at atmospheric pressure both experimentally and numerically, using the system-scale code CATHARE. Low-pressure loops are prone to instability due to strong differences of density between the liquid and the vapor. Particular attention is devoted to analyzing the boundaries of the flow reversal regime with respect to flow cross section aperture (related to friction forces and experimentally performed using regulation valves) upstream and downstream of the heated test-section. At low heat flux, the flow is stationary, whereas at higher heat flux, flow reversal appears. The system-scale code is amenable to reproduce the flow reversal regime boundaries explored experimentally. An analytical criterion is used to highlight that boiling may become unstable and flow reversals appear. Results show that the stable flow region boundaries can be extended by increasing the upstream pressure loss coefficient (valve closing) in order to reach large exit void fractions $\alpha \approx 1$. In configurations where the upstream pressure losses dominate, stable boiling points with high mass flux and high heat flux are observed. On the opposite, larger downstream pressure loss coefficients strongly favor instability and flow reversal.

Keywords: Natural circulation, thermal-hydraulics, stability, experiment, system-scale code, pressure losses

---

1. Introduction

Natural circulation loops are of huge importance in engineering, in particular for nuclear safety, as they can be used to remove heat in a system without active mechanical devices. This provides inherent robustness as there are no active parts (pump) and raises strong interest for nuclear safety applications. Such systems are prone to flowrate instability [1], which can be of multiple types [2]. In the case of a vertical heat exchanger, if the flow remains single phase, the system is stable. However, if boiling occurs, unstable mechanisms may lead to system instability (without reversals) and possibly flow reversals [3, 4]. In the case of nuclear safety, such instabilities might have thermomechanical consequences on the heat exchanger. One characteristic of the studied natural circulation loop is that the operating pressure is close to the atmospheric pressure. Achieving stable boiling would be a way to benefit from the latent heat of water and improve the heat removal. Experimental campaigns on test loop are an opportunity to study the hydraulic design of the loop in these conditions. Concretely, this means that the effect of pressure losses on stability boundaries needs to be evaluated. The system considered here is a model system. The heating is simplified to direct electrical heating, and the thermal heat flux is thus imposed.

2. State of the art

Several mechanisms of instabilities are described in the literature, by experimental methods or theoretical analyses [2, 5–9], and stability maps for natural circulation systems can be obtained [4, 10–12]. In each case, the boundaries are system-dependent. In facilities where the riser length is large compared to the test-section length, flashing instabilities can be the dominant instability mechanism [13]. In other cases, flow regime transitions can be at the origin of flow instability [14]. The pioneer work of Ishii [10] has lead to determining a stability criterion for Density Waves Oscillations (DWO) which depends mainly on the upstream and downstream pressure loss coefficients.

Fukuda and Kobori further classified DWO into two types [15]. The Type I oscillations occur at low exit quality, where the gravitational pressure drop over the riser (unheated vertical part after the test-section) plays a major role. The Type II occurs at larger qualities. In this case the frictional pressure drop is the dominant mechanism of instability. Rohatgi and Duffey [16] derived a simplified stability criterion, based on the pressure equation over the loop. Guanghi et al. [17] performed a linear stability analysis and provided an explicit equation for the growth rate of the instability. This criterion is used here to assess the effect of inlet and outlet singular pressure losses.

A particular type of instability is the flow reversal instability which is typically observed in small diameter channels [18], and is due to a sudden vapor expansion. Brutin et al. [19] showed experimentally that the growing vapor pushed the liquid back to the inlet, where a buffer tank was placed. Jones and

---

[*] Corresponding author
Email address: `sebastien.renaudieredevaux@cea.fr`
(S. Renaudière de Vaux)

Nomenclature

Abbreviations and acronyms

MAE	Mean Absolute Error
ME	Mean Error
RMS	Root Mean Square
CEA	Commissariat à l'Énergie Atomique et aux Énergies Alternatives
CHF	Critical Heat Flux
CL, HL	Cold Leg, Hot Leg
DWO	Density Waves Oscillations
PWR	Pressurized Water Reactor

Greek letters

α	Void fraction
κ	Heat diffusivity, [m^2/s]
μ	Dynamic viscosity, [Pa.s]
ρ	Density, [kg/m^3]
σ	Surface tension, [N.m]
ξ	Pressure loss coefficient

Latin letters

A	Area, [m^2]
a_i	Coefficient of the polynomial fit for the valve pressure loss coefficient
C_1 to C_5	Empirical coefficients
C_m	Multi-phase multiplier
c_p	Heat capacity of liquid, [J/K]
D, d	Diameter, [m]
f_s	Single-phase regular friction coefficient
G	Mass velocity, [kg/(m^2.s)]
g	Gravitational acceleration, [9.81 m/s^2]
h	height, [m]
h_{lv}	Latent heat of vaporization, [J/kg]
P, ΔP	Pressure and pressure difference, [Pa] or [bar]
Q	Mass flowrate, [kg/s]
q''_{in}	Wall heat flux, [W/m^2]
T	Temperature, [°C]
U, u	Velocity, [m/s]
x	Vapor quality

Nondimensional numbers

Bo	Boiling number, $\frac{q''_{CHF}}{Gh_{lv}}$
N_{pch}	Phase-change number, $\frac{q''_{in}A_w}{GA_c h_{lv}}\frac{\rho_l-\rho_v}{\rho_v}$
N_{sub}	Subcooling number, $\frac{c_p(T_{sat}-T_{in})}{h_{lv}}\frac{\rho_l-\rho_v}{\rho_v}$
Re	Reynolds number, $4Q/(\pi D\mu)$
We	Weber number, $G^2d/\rho_l\sigma$

Subscripts

atm	atmospheric
c	cross-section
in	inlet
l	liquid phase
out	outlet
probe	probe
reg	regular
sat	property at saturation
sing	singular
v	vapor phase
valve	relative to the valve
w	wall

Judd [20] assumed that the repeated dryout and rewetting of the wall caused the onset of the critical heat flux (CHF).

These reversals were observed experimentally in a parallel four-channel system at low pressure 1-10 bar [3]. The authors observed at 9 bar flow oscillations without reversals, whereas at 1 bar flow reversal appeared, highlighting the destabilizing effect of low pressure, also observed in other facilities [14]. Moreover, at low pressure the vapor reached the entrance of the channels and caused the instability to propagate to the neighboring channels.

Recently, Chen et al. [4] analyzed the flow reversals in a loop with a cylindrical test-section. They attributed the reversals to premature apparition of the CHF, due to flowrate oscillations that lead to large wall temperature increase. Similar behavior was observed in a rod-bundle test-section [21]. The CHF can be estimated thanks to the correlation from [22, 23] and will be discussed later in the paper. The system-scale code RELAP5 was used in an external vessel cooling configuration and highlighted flow reversals [24]. The system-scale code RELAP5 has also shown good results in reproducing the oscillatory behavior (without flow reversal) at low pressure in a rod bundle configuration [21]. We focus here on the effect of pressure losses on flow reversal boundaries, using experiments and system-scale simulations.

In the case of nuclear safety, system-scale codes are used to predict the mass flux. System-scale codes have demonstrated their ability to predict quantitatively flow stability in natural circulation [21, 25–27]. The CATHARE code [28–31], used in this study, is based on a two-fluid, six-equation model [32]. The two-phase and phase change closure laws have been mainly validated for high operating pressures, i.e. PWR conditions in the primary circuit. In order to validate the stability results at atmospheric pressure, a dedicated circulation loop, called EXOCET, has been designed and built at CEA[1] Cadarache to study the effect of pressure losses on the stability boundaries. In parallel, a numerical model of the loop was developed using the CATHARE code. In a previous work, experimental stability maps from [4] were reproduced successfully with the numerical model [27].

Several issues are at stake. First, we present the experimental setup and introduce the numerical model based on the CATHARE code. Then we discuss the stability criterion from Guanghi et al. [17] and evaluate the pressure losses of the current loop and the CHF. Second, the system-scale code is compared to experimental data in low-pressure natural circulation loop, in order to extend its validation domain. Finally, stability boundaries are then determined as a function of the upstream and downstream pressure losses, respectively called ξ_{in} and ξ_{out}. The boundaries are then compared to CHF values. Quantification of the influence of pressure losses on the boundaries is shown, as it is of strong interest in the context of nuclear design. In addition, possibilities of stable flow boiling at low pressure will be highlighted.

3. Experimental and numerical methods

3.1. Experimental facility: EXOCET rig

The experimental facility EXOCET, built in CEA Cadarache is sketched in Fig. 1. It is designed with large pipes compared to the test-section to get negligible frictional pressure drop in the pipes outside the test-section. Two regulated valves are added upstream and downstream the test-section to permit to change pressure loss coefficients upstream and downstream the test-sections. The heating of the test-section pipe is performed by a direct electrical heating of adjustable power within the range 0-50kW. Compared to fluid-fluid heat exchangers, this is a simplification that allows to control precisely the power input, independently of the flowrate. The test-section is insulated to prevent heat losses and electrical short-cuts. The pipes upstream and downstream the test-section are also thermally insulated to prevent heat losses. Moreover, the external side of the CL and HL is thermally insulated[2]. Figure 2 gives photos of the rig. The large electrical connection in copper permits to get an uniform distribution of the electrical current at the inlet and outlet. The tank can be pressurized to simulate different height of water. The temperature of the test-section is measured with 54 thermocouples (distributed along 3 azimuths and 18 heights) on the outside wall of the test-section's tube. They are thermocouples of type K (0.8mm diameter with an accuracy of ± 1°C). The mixture temperature is measured within the pipes at different positions (see Fig. 1) using platinum probes (Pt100) with an accuracy of ± 0.1°C. A Coriolis flowmeter measures positive and negative flowrates with an accuracy of ± 0.002 kg/s within the range -0.2 kg/s to 0.5 kg/s. Pressure transducers have an accuracy of ± 2 mbar for absolute pressure measurements and ± 1 mbar for differential measurements. During measurements, a visualization window permits EXOCET's pilots to get a qualitative insight of the two-phase flow.

Throughout the whole study, the water level is imposed at $h_{water} = 2$ m within the tank. Above the water level, the atmospheric pressure is $P_{atm} \approx 1$ bar. A heat exchanger permits the regulation of the water temperature within the range 20°C to 80°C. It ensures that at the exit of the tank, the water reaches the desired temperature T_{in}.

A pump (implemented at the entrance of the cold leg) permits to characterize the pressure loss coefficients of the valves ξ_{in} in the cold leg (CL) and ξ_{out} in the hot leg (HL). For natural convection experiments, the pump is bypassed thanks to two valves. A flowmeter in the CL is used to measure the mass flowrate. Both the CL and the HL have circular cross-section with constant diameter D. The vertical heated section has a diameter 5 times smaller than the one of the pipes of the CL and HL. Main characteristics of the EXOCET rig are summarized in Tab. 1 for geometry, Tab. 2 for physical parameters, Tab. 3 for sensors and their accuracy.

3.2. Characterization of pressure drop coefficients

The singular pressure losses of the valves are given by:

$$\xi_{in} = \frac{\Delta P_{valve,in}}{\frac{1}{2}\rho U^2} \tag{1}$$

$$\xi_{out} = \frac{\Delta P_{valve,out}}{\frac{1}{2}\rho U^2}, \tag{2}$$

with $\Delta P_{valve,in}$ and $\Delta P_{valve,out}$ the valves pressure drops and U the water velocity in the CL and HL. The coefficients are estimated as a function of the valves opening using pressure drop measurement with different mass flowrates[3] Q and Reynolds number $Re = 4Q/(\pi D \mu)$. The results are given in Fig. 3 along with the manufacturer data (blue diamonds in Fig. 3).

A 3rd order polynomial approximation of $\log_{10}(\xi_{in})$ and $\log_{10}(\xi_{out})$ is performed:

$$\log_{10}(\xi_{in}) = \sum_{k=0}^{3} a_i X_{in}^i \tag{3}$$

$$\log_{10}(\xi_{out}) = \sum_{k=0}^{3} a_i X_{out}^i \tag{4}$$

with the a_i given in Tab. 4, and X_{in} and X_{out} are the valve openings in percentage. The polynomial function fits well with the

---

[1] Commissariat à l'Énergie Atomique et aux Énergies Alternatives (French Atomic Energy Commission).

[2] It was checked during the characterization trials that the overall temperature loss between the inlet of the CL and the outlet of the HL was below 2°C. During the natural circulation experiments, the difference between the temperature at the inlet of the CL and the inlet of the test-section is always below 1°C.

[3] provided by the pump, i.e. forced convection of liquid water

experimental data and manufacturer data. Indeed, most of the measurements fall in the red shaded area, which represents a ±10% difference with respect to equations (3) and (4).

It is seen that the upstream and downstream valves have a similar behavior. For fully open valves, singular loss coefficients show that $90 \leq \xi_{in}, \xi_{out} \leq 200$. These values are higher than what could be expected from an open valve which is generally close to unity [33]. This is due to the inner diameter of the valves pipe d_{valve}, which is smaller than HL and CL inner diameters D. As ξ_{in} and ξ_{out} are based on the velocity in the HL and CL $U = 4Q/(\rho\pi D^2)$, and not on the velocity in the valve pipe $u = 4Q/(\rho\pi d^2_{valve})$. The measured value ξ_{in} and ξ_{out} based on the HL or CL velocity is then higher then the value based on the velocity inside the valve by a factor $D^4/d^4_{valve} \approx 40$. The uncertainty range is given by the grey shaded area in Figs 3. The upper limit is around $\approx 10^3$ for both ξ_{in} and ξ_{out}. We also observe that the data have a wide dispersion for openings $\lesssim 30\%$. This due to temporal fluctuations linked with fluid-valve interaction.

The singular losses coefficients then increase as the valve is further closed. In particular, for 60% opening, we have $\xi_{in}, \xi_{out} \approx 10^3$ and for 40% opening, we have $\xi_{in}, \xi_{out} \approx 10^4$. For opening values as low as 20%, a drastic increase is observed, where the coefficients reach values close to 10^6. Closing the valves also induces an increase in data dispersion. Lower opening values could not be obtained in order not to damage the loop. We also note that there is no influence of the mass flux (i.e. Reynolds number Re) on these values, consistently with literature [33].

3.3. Experimental approach of flow instabilities

The stability boundaries are experimentally determined using the following method. An example is shown in Fig. 4. First at static equilibrium and fully open valves, the heat flux q''_{in} is gradually imposed in the wall, and reach the desired value of q''_{in} (around 500 s in Fig. 4). Circulation sets in and after a transient regime, a steady-state is reached. Then the valve is further and further closed, until flow reversal appears. In Fig. 4, flow reversal is reached around 1700 s, for a valve opening between 40 (before the reversal) and 35% (after the reversal). It is assumed that at first order, the reversal appears at the medium value of the valve opening, which is 37.5% in this case. The uncertainty margin is discussed in Section 5.1. Far beyond the stability boundary, quick rises in the wall temperature > 40°C/s led to stop the experiments as the wall power is imposed. This is different from heat exchangers of usual passive systems, where the maximal wall temperature is limited by the hot fluid temperature. The experimental stability diagram is constructed by repeating this method for several values of (q''_{in}, T_{in}).

The computed mass velocity $G = Q/(\pi d^2/4)$ is also shown in Fig. 4. Contrary to the experiment, the flowrate sets in progressively between $t = 0$ and 500 s. This discrepancy is explained by the sensitivity of the flowmeter, as discussed in the following paragraph. The flowrate decreases as the valve is closed and the flow reversal appears earlier in the computation, around $t = 1600$ s and at 40% of valve opening. Moreover, for each step, the computed flowrate is higher than the measured one in this case. The experimental vs. numerical differences for all cases are discussed in Section 5.1.

Experimentally, no influence of ξ_{in} was observed on the flow reversals in the investigated range. This configuration is shown in Fig. 5 where the upstream valve was closed step-by-step. The numerical model and results are discussed later in the paper. As expected from the valve characterization, no significant effect of the valve opening was observed between 100% and 70% opening. When the upstream valve was further and further closed from 70% to 30%, the flowrate decreased slowly at first, from 390 kg/m^2.s to 310 kg/m^2.s. Then when the opening reached 30% (around $t = 3250$ s), a zero flowrate is measured. The computed G is also shown in Fig. 5. There is a very good agreement in the steady flowrate regime. However, when the circulation stops experimentally, this effect is not observed numerically. Indeed, the flowrate decreases as the valve is further closed. In such case, it is observed that ΔP_{CL} still varies when the upstream valve is further closed. This indicates that there is circulation in the CL. The flowrate can be estimated in the CL by the momentum conservation:

$$\rho_l g(z_0 - z_1) - \Delta P_{CL} = \rho_l \xi_{CL} \frac{U^2}{2}, \tag{5}$$

where $z_0 - z_1$ is the height difference between the inlet and exit of the CL, and ξ_{CL} is the pressure loss coefficient of the CL. It is defined later in the paper, in Eq. (6). The mass velocity estimate from (5) is shown in Fig. 5 and is approximately half of the value from direct flowrate measurement and computation. For $t \geq 3300$ s, the estimate from (5) shows that there is still circulation with $G \approx 100$ kg/m^2.s and points to a measurement limitation. However, due to uncertainties on ΔP_{CL} and ξ_{CL}, it is not possible to use this estimate quantitatively, and these points are not considered for the analysis. The absence of measured flowrate is here likely due to the sensitivity of the flowmeter. The zero flowrate is also observed in the early phase of the test, between t =0 s and 500 s, as shown in Fig. 4. As a consequence, the early stage of the trials cannot be interpreted further.

3.4. Modeling with the system-scale code CATHARE

A numerical model of the EXOCET loop was developed with the system-scale code CATHARE, which is based on a two-fluid six-equations model [29, 32]. Valves are modeled by singular pressure losses with prescribed coefficients ξ_{in} and ξ_{out}. The code uses finite volumes for the vapor and liquid velocities, and finite differences for the other variables, with a staggered mesh and the donor cell principle. Time-integration is performed with an implicit scheme. The nonlinear system of equations is solved by a Newton-Raphson iterative method following several steps. It was verified that mesh convergence was achieved for the parameter range. A view of the numerical model of EXOCET is shown in Fig. 6, where the numerical mesh is seen. The radial heat conduction in the wall is taken into account over three cells distributed between d and the outer diameter d_{ext}. We consider that there is no heat transfer to the exterior medium.

Numerically, the flow is initialized with rest flow conditions and thermal equilibrium, with values of ξ_{in} and ξ_{out} corresponding to the experimental values. A linear power ramp is imposed during 500 s to reach the desired q''_{in}, and after a transient regime, a steady-state is reached. Four types of regimes were identified:

1. Stable: At low q''_{in}, the flowrate reaches a constant value over time;
2. Oscillatory: when q''_{in} is increased, the flow becomes weakly unstable, and oscillations appear without flow reversals. This regime is defined arbitrarily with the condition that the standard deviation of $G(t)$ is above 5% of the time-average mass flow value G_{av}. This regime is rarely observed here;
3. Reversals: when q''_{in} is further increased, oscillations are stronger and flow reversals ($G < 0$) appear;
4. Reversals and computation stop: depending on the flow dynamics and wall dryout, it led in some cases to large increase in wall temperature or pressure increase. It resulted in computation stop due to the wall melting point that was reached, or an impossibility for the code to converge. This is in agreement with the experiments in presence of dryout, where the wall temperature increases due to the direct electrical heating.

Several sets of simulations were run. First, all experimental transients were reproduced in order to validate the code in the stable regime. They are discussed in Section 5.1. Second, several batches of simulations were carried out, in order to determine the numerical stability boundaries as a function of ξ_{in} and ξ_{out}. The results are discussed in Section 5.2 Each batch of simulations is carried out with fixed values of ξ_{in} and ξ_{out}. Their values are taken from a grid, constituted of $\xi_{in} = [1, 10^2, 10^3, 10^4]$, and $\xi_{out} = [1, 10^2, 10^3, 10^4, 10^6]$. This represents a total of $4\times5 = 20$ batches of simulations. Similarly, the values of the input parameters (q''_{in}, T_{in}) are varied within a batch and based on a linearly spaced grid, constituted of a total of $14 \times 14 = 196$ points, in the range $59\ \mathrm{kW/m^2} \leq q''_{in} \leq 236\ \mathrm{kW/m^2}$ and $20°\mathrm{C} \leq T_{in} \leq 80°\mathrm{C}$.

4. Analytical background

In this Section, we discuss the main nondimensional parameters governing the onset of flow reversals. A link with the onset of CHF is made in regard of the defined parameters.

4.1. Analysis of frictional pressure losses

For the CL and HL, the global frictional pressure loss coefficients can separated into three contributions :

$$\xi_{CL} = \xi_{in} + \xi_{reg,CL} + \xi_{sing,in} \tag{6}$$

$$\xi_{HL} = \xi_{out} + \xi_{reg,HL} + \xi_{sing,out} \tag{7}$$

where $\xi_{reg,CL}$ and $\xi_{reg,HL}$ represent the regular friction losses in the CL (single-phase) and the HL (two-phase). The interfacial friction is omitted here as they are a consequence of the two-phase flow and are accounted for in the code, as well as the gravitational pressure losses. These terms are given by:

$$\xi_{reg,CL} = f_s \frac{L_{CL} + h_{in}}{D}, \tag{8}$$

$$\xi_{reg,HL} = f_s C_m \frac{h_{out} + L_{HL}}{D}, \tag{9}$$

with L_{CL} and L_{HL} the total pipe length of the CL and HL, respectively. the coefficient f_s is the single-phase regular friction law in the test-section coefficient, and $C_m \approx 2$ is a good approximation for the multiphase multiplier. In the laminar regime, $f_s = 64/Re$. In the turbulent regime $Re \geq 10^3$ we use the Blasius friction law [34] $f_s = 0.316/Re^{0.25}$ in order to follow the model included in the CATHARE code. For the investigated range, $0.03 \leq f_s \leq 0.05$. The regular friction coefficients were here $\xi_{reg,CL}, \xi_{reg,HL} \leq 10$ in all cases. Therefore, for $\xi_{in}, \xi_{out} \geq 100$, we consider that the regular pressure losses are negligible, and that the CL and HL total pressure losses are equivalent to the valves pressure losses. This is supported by the experimental measurements. Even though they are negligible, the regular pressure losses are still computed in the numerical model.

The coefficients $\xi_{sing,in}$ and $\xi_{sing,out}$ represent the other singular pressure losses, from elbows or diameter change at the inlet or outlet of the test-section. These terms depend on the geometrical characteristics only and are estimated using data from [33]. In the end, it is found that $\xi_{sing,in}, \xi_{sing,out} < 10$ and they can be neglected compared to the valves pressure losses.

Moreover, here the two-phase regular friction term inside the test-section is $4 < \frac{f_s C_m}{2d/h} < 7$, and is in general negligible compared to the equivalent pressure losses of the CL and HL, ξ_{in} and ξ_{out}. Finally, we consider that:

$$\xi_{CL} \approx \xi_{in} \tag{10}$$

$$\xi_{HL} \approx \xi_{out}. \tag{11}$$

4.2. Stability criterion

We consider the natural circulation loop shown in Fig. 1, whose dimensions are given in Tab. 1. An enthalpy balance on the heated test-section gives:

$$N_{pch} = N_{sub} + x_{out} \frac{\rho_l - \rho_v}{\rho_v} \tag{12}$$

where the phase-change number N_{pch} and the subcooling number N_{sub} are defined from [10] as:

$$N_{pch} = \frac{q''_{in} A_w}{G A_c h_{lv}} \frac{\rho_l - \rho_v}{\rho_v}, \tag{13}$$

$$N_{sub} = \frac{c_p (T_{sat} - T_{in})}{h_{lv}} \frac{\rho_l - \rho_v}{\rho_v}, \tag{14}$$

with:

- $A_w = h\pi d$, $A_c = \pi d^2/4$: wall surface and cross-section;
- T_{sat}, T_{in}: saturation and inlet temperatures;

- ρ_l, ρ_v: liquid and vapor densities;

- c_p: heat capacity of the liquid;

- h_{lv}: latent heat of vaporization;

- x_{out}: vapor quality at the exit of the test-section.

The two-phase portion of the (N_{pch}, N_{sub}) plane is bounded by the boiling boundary $x_{out} = 0$ (or equivalently $N_{pch} = N_{sub}$) and by the $x_{out} = 1$ line. The latter boundary is given here by $N_{pch} = N_{sub} + \dfrac{\rho_l - \rho_v}{\rho_v} \approx N_{sub} + 1600$. We investigate the effect of upstream and downstream pressure losses on the stability diagram. The stability of two-phase natural circulation was studied in depth by Ishii [10] for forced circulation. He derived an analytical stability criterion based on a drift-flux analysis. It accounts for geometrical characteristics and several dynamic contributions, essentially from drift flux and gravitational forces. A simplified version was also derived, which only depends on geometrical properties (i.e. pressure losses). This criterion constitutes a sufficient criterion for stability. It highlights the stabilizing effect of ξ_{in} and the destabilizing effect of ξ_{out}.

Guanghi et al. [17] derived an analytical criterion based on a homogeneous model. They also neglected the subcooled region but took into account the singular losses at inlet and outlet of the loop. For natural circulation, the typical marginal stability boundary is illustrated in Fig. 7a. Schematically, four typical boundaries, labelled $x_{out} = 0$, A, B and C, are defined. The Type I instability is bounded by the curve labelled A; the Type II is bounded by B and C.

These boundaries are dependent of the investigated system. In the EXOCET configuration, the marginal stability lines are shown in Fig. 7b for a given $\xi_{out} = 10^2$ and various values of ξ_{in}. The boundaries are straight lines that delimit stable and unstable zones, labelled S and U in Fig. 7b. A zoom on the region of interest for EXOCET is presented in Fig. 7c. First the boundaries A and B are not influenced by the value of ξ_{in}. Second the maximal achievable subcooling number in the EXOCET conditions is $N_{sub,max} \approx 300$. This limit is obtained by the freezing temperature of water, i.e. $T_{in} = 0$°C. In practice, for $N_{sub} \leq N_{sub,max}$, boundaries A and B collapse to the boiling line $x_{out} = 0$, i.e. $N_{sub} = N_{pch}$. Consequently:

- the unstable zone between $x_{out} = 0$ and A is difficult to observe in practice;

- and the stable zone between A and B is difficult to observe in the EXOCET configuration.

The collapse of A and B towards $x_{out} = 0$ is due to the small riser length $h_{out} = 0.6$ m, compared to the test-section height $h = 2.7$ m. Hence, the DWO unstable zone for EXOCET is bounded by the triangle formed by $x_{out} = 0$, $N_{sub,max} \approx 300$ and line C.

Second, the boundary C depends on the inlet and outlet pressure losses. In particular, the inlet singular pressure loss ξ_{in} favors stability. For $\xi_{in} = 1, 100$ and 10^3, the boundaries are quasi-merged into a common line. For $\xi_{in} = 10^4$, the boundary C is higher. In the EXOCET configuration, N_{sub} and N_{pch} vary from 50 to 200 approximately, represented by the grey shaded square in Fig. 7c. The increase in ξ_{in} moves boundary C upwards, leading to a reduction of the unstable triangle with regards to DWO. In fact, for $\xi_{in} = 10^4$, line C is practically out of the region of interest. The stabilizing effect of ξ_{in} has been highlighted in [14] for $1 \leq \xi_{in} \leq 146$.

4.3. CHF estimate

The CHF in a vertical upward flow is here estimated using the inlet conditions given by the correlation from [22, 23], which validity domain covers our conditions in terms of operating conditions (flowrate, pressure, subcooling) and geometry (pipe diameter and height). It is directly expressed from:

$$Bo = \frac{q''_{CHF}}{G h_{lv}} = \frac{C_1 We^{C_2} \left(\rho_l/\rho_v\right)^{C_5} \left[1 - C_4 \left(\rho_l/\rho_v\right)^{C_5} x_{in}\right]}{1 + 4 C_1 C_4 We^{C_2} \left(\rho_l/\rho_v\right)^{C_3 + C_5} (h/d)} \tag{15}$$

with the boiling number Bo, the Weber number $We = G^2 d / \rho_l \sigma$, the inlet quality x_{in}, $C_1 = 0.0722$, $C_2 = -0.312$, $C_3 = -0.644$, $C_4 = 0.900$ and $C_5 = 0.724$. As equation (15) requires to know the mass flux G, interpolation near the flow reversal boundary is difficult. We point out that the CHF is computed in the CATHARE code thanks to the CHF look-up table of Groeneveld et al. [35]. Using Eq. (15), the CHF in the investigated range is $50\text{kW/m}^2 \leq q''_{CHF} \leq 220\text{kW/m}^2$, which is similar to the investigated q''_{in} range.

Equation (15) can be reformulated in terms of a phase-change number where CHF occurs, as a function of We and N_{sub}:

$$\begin{aligned} N_{pch}^{CHF} &= \frac{A_w}{A_c} \left(\frac{\rho_l - \rho_v}{\rho_v}\right) \\ &\times \frac{C_1 We^{C_2} \left(\rho_l/\rho_v\right)^{C_5} \left[1 - C_4 \left(\rho_l/\rho_v\right)^{C_5} \left(\frac{\rho_l - \rho_v}{\rho_v}\right) N_{sub}\right]}{1 + 4 C_1 C_4 We^{C_2} \left(\rho_l/\rho_v\right)^{C_3 + C_5} (h/d)} \end{aligned} \tag{16}$$

The CHF line computed from (16) is shown in Fig. 8 for several values of N_{sub} for several values of G, with the boiling line $N_{pch} = N_{sub}$. At constant G, equation (16) is represented by a straight line. Here, the G values are assumed constant to emphasize the evolution at imposed G. This differs from natural circulation where G is the result from the interaction between the driving term q''_{in} (buoyancy) with the pressure losses (ξ_{in} and ξ_{out}). In the next Section, G values will be taken from CATHARE simulations, which include the ξ_{in} and ξ_{out} effects on the mass velocity. The CHF estimates therefore include the effect of pressure losses on the observed flowrate.

First, it is observed that the CHF line is close to the boiling line for all G values. Second, for $N_{sub}/N_{pch}^{CHF} < 1$ nucleate boiling occurs before the onset of CHF, whereas for $N_{sub}/N_{pch}^{CHF} > 1$ boiling occurs directly in the CHF regime.

The transition N_{sub} decreases with the mass flow G from $N_{sub} \approx 150$ at $G = 300$ kg/m^2.s to $N_{sub} \approx 50$ at $G = 1100$ kg/m^2.s. In conclusion, the nucleate boiling region (between the dashed line and the straight line) is very narrow in low pressure conditions, and the onset of CHF occurs quickly after the inception of boiling. Here, the reaching of the CHF is due to the denstiy ratio. The boiling of liquid generates a large volume of vapor as $\rho_v/\rho_l \approx 10^{-3}$, which occupies the width of the channel.

As it will be seen in the following Section, the CHF plays a key role on the stability boundaries. In the simulations, G is a function of N_{pch} and N_{sub}, so the representation of equation (16) is not necessarily a straight line.

5. Results and discussion

We first validate our results in the stable regime. Then experimental and numerical stability boundaries are given and discussed.

5.1. Code validation in the stable regime

In the stable regime, the flow reaches a steady state both experimentally and numerically for given values of T_{in} and q''_{in}. All experimental transients are reproduced numerically. The downstream valve is closed step-by-step and a succession of steady states is observed, until the apparition of flow reversals. After stabilization at each valve closing, the steady values of T_{out} and G are averaged over 50 s, sampled at 1 Hz. Their temporal variations are characterized by their root mean square (RMS) value. For the temperature measurements, the RMS values are below the uncertainty error. The comparisons of the measured and computed values of the mass velocity G and $\Delta T_{out}/\Delta T_{sat} = (T_{out} - T_{in})/(T_{sat} - T_{in})$ are given in Fig. 9, with T_{out} the temperature at the exit of the test-section. The stable values of the mass velocity vary from $G = 300$ kg/m^2.s to 800 kg/m^2.s and the temperature variation is $0.5 \leq \Delta T_{out}/\Delta T_{sat} \leq 1$. For the mass velocity G, two groups of data are observed. First, a group with less than 10% difference with experimental data is observed, with 300 kg/m^2.s$\leq G \leq 400$ kg/m^2.s. The second group displays differences from 10 to 20%, and ranges from 350 to 700 kg/m^2.s. For the temperature difference, the relative difference if lower than 5% for all cases. This shows a very good agreement of computations with experimental data in the stable regime. It is also noticed in Fig. 9, that the second group has larger temporal fluctuations than the first one. These oscillation might be linked with Type I DWO (see Fig. 7a). The difference in measured and computed pressure losses are below 0.02 bar for the CL, the test-section and the HL.

We define the mean error (ME), mean absolute error (MAE) and root mean square (RMS) error, between an experimental quantity X_{exp} and a computed quantity X_{calc} as:

$$ME = \frac{1}{N}\sum_i \frac{X_{i,calc} - X_{i,exp}}{X_{i,exp}}, \quad (17)$$

$$MAE = \frac{1}{N}\sum_i \left|\frac{X_{i,calc} - X_{i,exp}}{X_{i,exp}}\right|, \quad (18)$$

$$RMS = \sqrt{\frac{1}{N}\sum_i \left(\frac{X_{i,calc} - X_{i,exp}}{X_{i,exp}}\right)^2}, \quad (19)$$

where $X_{i,exp}$ and $X_{i,calc}$ are the ith observation of X_{exp} and X_{calc} respectively; and $N = 100$ is the total number of observations. Some characteriscs of these operators can be noticed:

- $MAE \geq ME$: The mean absolute error is always greater than the mean error;
- if $MAE \approx ME$ (hence $ME \geq 0$): the code tends to overpredict the quantity X;
- reversely if $MAE \approx -ME$ (hence $ME \leq 0$): the code tends to underpredict the quantity X;
- if $ME \approx 0$ and $MAE > 0$: The code tends to overpredict or underpredict X, without a clear tendency, and is accurate on average.

The RMS error emphasizes the large deviations. If $RMS \approx MAE$, the deviations are not significantly larger than the MAE, and there are no significantly large deviations. The values of the error indicators are summarized in Tab. 5 for $\Delta T_{out}/\Delta T_{sat}$, the mass velocity G and the pressure losses of the CL, test-section and HL. The values are around 5% for $\Delta T_{out}/\Delta T_{sat}$ and around 10% for G, conformly to the results from Fig. 9. Moreover the ME for the temperature is close to 0%, which means that there is not clear tendancy to overestimate (or underestimate) this quantity. On the opposite for G, it is seen that $MAE \approx ME$, and the code generally overestimates the mass velocity. The regular overestimate of the flowrate is due to the neglected thermal losses in the test-section in a first approach. For the CL and TS pressure losses, the errors are around 10%, while they are around 100% for the HL. The larger deviation for the HL is due to very low pressure losses in this section. Indeed, for all cases, the HL losses are below 0.02 bar. The typical deviation in absolute values for the pressure losses is around 0.02 bar for all cases. The HL pressure losses ΔP_{HL} are measured thanks to two pressure sensors, with uncertainty of ±2 mbar, as given in Tab. 3. The uncertainty on ΔP_{HL} is therefore ±4 mbar. It is too close to the measured values to conclude further on the experiment vs. simulations ΔP_{HL} in the HL. In addition, in a horizontal pipe with diameter $D = 0.10$ m, there is a hydrostatic pressure gradient $\Delta P \approx \rho_l g D = 10$ mbar between the top and bottom of the pipe. In the 1D modeling, a homogeneous pressure is assumed over the cross-section. This further limits the interpretation of low pressure losses in horizontal pipes with large diameters.

5.2. Stability boundaries

For a given set of (ξ_{in}, ξ_{out}), the flow is stable at large subcooling numbers N_{sub} and low q''_{in}. It becomes unstable if q''_{in} is increased beyond a maximal value, or if N_{sub} is decreased below a critical value. As seen from the literature, the boundary between the stable and unstable regime is given by a straight line in the (q''_{in}, N_{sub})-plane [4, 10–12, 24]. This boundary is however system-dependent, i.e. it depends on the geometry and on the system pressure losses. Reversely, if one remains at constant q''_{in} and N_{sub}, but changes the values of ξ_{in} or ξ_{out} as done here, instability will set in. The experimental stability boundaries are given in Fig. 10. They are interpolated from the experimental data points shown in the graph. For given valve opening, the boundary is given by the corresponding line, and the flow is stable above it and unstable below it. At fully open valve

$\xi_{in} \approx 10^2$, the boundary is in the lower right corner of the graph. When the valve is further and further closed, the boundary remains a straight line but is pushed toward the upper left corner of the graph. Below openings of 30% ($\xi_{in} \approx 10^{4.5}$), no experimental data could be acquired, as flow reversal immediately appeared. The experimental boundaries also highlight the weak influence of the valve for openings larger than 60% ($\xi_{in} \leq 10^3$) as the boundaries remain close to each other. For lower values of the valve opening ≤ 50% ($\xi_{in} \approx 10^{3.5}$), the boundaries are more and more spaced, showing the growing influence of closing the downstream valve on the stability diagram. The observed boundaries are straight lines, in agreement with the literature results in similar configurations [4, 11, 12, 21, 24, 36]. A source of uncertainty is that ξ_{out} was measured in a single-phase flow, whereas in natural circulation a two-phase flow might occur in the HL. However, as it is discussed later, the stability boundaries are similar to the inception of boiling, which limitates the uncertainty.

5.3. *Oscillatory regime*

In Fig. 11, time-evolutions of the experimentally measured mass flux and temperature at the test-section exit are presented in a flow reversal configuration, and compared with the numerical results from CATHARE. It is seen that the mass flux and temperature oscillations are periodic in both cases. The numerical simulations show a behavior which is similar to experimental observations from [4] at the onset of flow instability. The results show an alternating of stable phases (labeled B and delimited by the grey area in Fig. 11) with rapid oscillations (labeled A). The duration of each phase is approximately 20 seconds. At the beginning of an oscillation cycle, the mass flux is steady. Then oscillations in mass flux of amplitude ±5000 kg/(m^2.s) appear due to quick vapor growth. Then the flowrate returns to a steady state and the cycle repeats.

The oscillation period is similar in simulations and experiments, and is around 40 seconds (cycle of A and B regimes). Simulations show large amplitude peaks, whereas experiments only show variations in the measurable range of the flowmeter (shown in Fig. 11), which is below the oscillation amplitudes (see Table 3). Moreover, the sampling rate of the flowmeter and the temperature probe is 1 Hz. This prevents measuring the rapid flowrate and temperature oscillations observed in the simulations. In addition, for the temperature measurements, a Pt100 probe of diameter $d_{probe} = 3$ mm was used. Conduction in a rod is stationary and established when $t \gg \tau_\kappa$ with $\tau_\kappa = d^2_{probe}/\kappa$ the characteristic thermal conduction time in the probe. Here, we have $\tau_\kappa \approx 0.72$ s and therefore the quick thermal oscillations $\lesssim 1$ s cannot be measured. However it is noticed than between the cycles, the temperature slowly increases and this phenomenon is well observed numerically.

Profiles over the heated section of void fraction α, liquid mass flux G_l and vapor mass flux G_v are shown in Fig. 12. The time scale is the same as in Fig. 11. First, for $t < 25.6$ s, the void fraction α is stationary, similarly to the flowrate (Fig. 11). It is zero at the bottom of the test-section until boiling occurs around $z \approx 3.0$ m and increases steeply to reach $\alpha \approx 0.7$ at the exit of the heated section. The vapor condensates and reaches $\alpha \approx 0.1$ at the test-section exit. At the beginning of the oscillation at $t = 29.8$ s, a vapor front propagates and expands towards the bottom. In consequence, the liquid is pushed back towards the inlet and $G_l < 0$ below the vapor front ($t = 30.4$ s). The absolute value of G_l increases as the front progresses. Above the front, there is almost no liquid, so $G_l \approx 0$. On the opposite, the vapor before the front flows upward and $G_v > 0$. At $t = 31.2$ s, the test-section is completly emptied, $\alpha \approx 1$ for $1\text{m} \leq z \leq 3.7$ m. The liquid velocity before the test-section is $G_l \approx -4500$ kg/m^2.s and then increases again for $t = 32.4$ s and after. This mechanisms repeats for three or four oscillations and returns to a steady behavior, and then the full cycle repeats with a 40 seconds period. The mechanism at play here is similar to the observations in small diameter channel from [19].

For higher q''_{in}, oscillations do not display a characteristic oscillation frequency. The code is able to capture qualitatively the successive flow reversals and their amplitudes. But it is not possible to interpret the data further, due to time-integration and sensitivity of the flowmeter. Numerically, the frequencies and amplitudes were find to strongly depend on T_{in} and q''_{in}.

5.4. *Comparison of experimental and numerical stability diagrams*

Figure 13 shows the numerical phase diagrams obtained with CATHARE. Each quadrant of the graph represents a given set of (ξ_{in}, ξ_{out}). A column represents a constant ξ_{in}, while a row represents a constant ξ_{out}. It is observed that numerically, ξ_{in} had no influence on the stability boundary in the (q''_{in}, N_{sub})-plane, while the ξ_{out} increase pushes the stability boundary to the upper left corner. This is in agreement with the experimental observations, given by the solid black lines, coming from the interpolation of experimental boundaries (Fig. 10). Similarly, the dashed black lines represent the upper and lower limits of the shaded area from Fig. 3. It is also noticeable that the oscillatory regime (without reversals) is rarely observed and only exists between the stable and reversal regime. This agrees with observations from [4].

For $\xi_{out} = 10^3$ and 10^4, the experimental boundary is in good agreement with the numerical boundary. For both cases, the flow reversal is anticipated by the CATHARE code with respect to the experiment. The upper uncertainty limit of +10% on the pressure loss coefficient exponent agrees well with the numerical boundary in both cases. The interpolated experimental boundary is a little lower than the numerical one. This is within the frame of the upper and lower uncertainty limits for $\xi_{out} = 10^4$. For $\xi_{out} \approx 10^3$, there is less influence on the boundaries, and the upper limit underestimates slightly the boundary. In both cases, the upper uncertainty limit of +10% on the pressure loss coefficient exponent frames well the boundary.

For $\xi_{out} = 10^6$, all simulations displayed flow reversals, consistently with experimental observations. The superimposed experimental stability curves for $\xi_{out} = 10^3$ and 10^4 show a good agreement with the numerical boundaries. Indeed, the boundaries are straight lines with similar slopes in both experiment and simulations. The discrepancy between experimental and numerical boundaries may be a consequence of the uncertainty on the measured values of ξ_{out}.

The red lines in Fig. 13 correspond to iso-values of $q''_{in}/q''_{CHF} = [0.95, 1]$, computed from equation (16). The flowrate values used for the CHF estimate were computed with CATHARE. The increase in ξ_{in} and/or ξ_{out} induce a decrease of G, and therefore a reduction of the margin to the CHF. The lines are in good agreement with the stability boundaries, and it shows that the flow reversal is due to the CHF apparition. We hereby confirm previous observations from [4] who also observed flow reversals and attributed it to CHF apparition. Unlike the results from [4], the flow oscillations without reversals is more difficult to observe here, probably due to the lower operating pressure (P_{atm} here against 3 to 5 bar in [4]). The agreement between the CHF apparition and the stability boundaries is less good when ξ_{in} dominates. This is due to the stabilizing effect of ξ_{in}, as seen for $\xi_{in} = 10^4$ and $\xi_{out} = 1$, 10^2 and 10^3. Here, the flow is stable in regions where $q''_{in}/q''_{CHF} > 1$. At low pressure, the quick vapor expansion with a large density ratio $(\rho_l - \rho_v)/\rho_v$ pushes back the liquid towards the inlet, as explained before (see Fig. 12). But when the upstream losses ξ_{in} are significant, the liquid flowing backward encounters resistance. The pressure from the vapor expansion is then not sufficient to sustain a backward flow. The forward flow then encounters resistance from the downstream losses ξ_{out}. The outcome (flow reversal or not) depends on the values of ξ_{in} and ξ_{out}. If ξ_{out} is small enough, the liquid still flows forward and now flow reversal is observed. Moreover, stable flow with $q''_{in}/q''_{CHF} > 1$ is only observed for $\xi_{in} = 10^4$. This is in good agreement with flow stabilization with the increase of ξ_{in}, as seen with the line C moving upward in Figure 7b.

Figure 14 shows the stable points from numerical simulations, colored by G_{av}, in the (N_{pch}, N_{sub})-plane. We point out that flow reversal points are not represented as the average mass flux G_{av} is difficult to interpret when the time-evolution of G displays large amplitude fluctuations. One observes that the points located above the boiling line defined by $N_{pch} = N_{sub}$, represented by the black dotted line, are stable. These points correspond to non-boiling cases, as seen from the enthalpy balance (12).

The CHF line is also represented in Fig. 14 by the solid blue line when data is available, and is almost coincident with the boiling line. This means that the CHF occurs almost as soon as boiling occurs. This explains why the oscillatory regime (without reversals) is highly difficult to observe. Indeed, it was seen in [4] that the oscillatory regime occurs in the boiling region $N_{sub} > N_{pch}$ but before the onset of CHF, $N_{pch} < N_{pch}^{CHF}$. As seen from Figs. 8 and 14, this region is very narrow at low pressure and hence highly difficult to observe. Moreover, the CHF curve is above the boiling line for $N_{sub} \geq 120$, conformly to Fig. 8. For these values, the onset of CHF prevents the boiling. Indeed, it is seen that the CHF line is the asymptotic limit of the numerical data points.

For cases where boiling occurs $N_{pch} < N_{sub}$, stable points exist. Moreover, these cases are located in the lower left corner, at $N_{pch} \leq 120$ and in the boiling region $N_{sub} < N_{pch}$, consistently with previous observations from Fig. 13. These cases only exist for low $\xi_{out} \leq 10^3$. Boiling increases the flowrate in this area, up to 900 kg/m^2.s, against 450 on the other side of the boiling curve. This constitutes a steep increase in G_{av}. This is also seen in Fig. 9, where α_{out} abruptly increases with T_{in}. This is also accompanied by an increase in the flowrate. The stability of flow in this area was also observed in [3, 4, 10–12, 36, 37]. They are located in the lower left corner of the graphs. Boiling is accompanied by a quick increase in flowrate as seen for $\xi_{out} = 1$, 10^2 or 10^3, in agreement¡ with observations from Fig. 13. The stable points disappear as ξ_{in} increases or ξ_{out} decreases.

For larger $\xi_{in} = 10^4$, the stable area is wider, up to $N_{pch} = 100$. This is in agreement with previous observations (Fig. 13) where stable flow exists even in the wall dryout regime $q''_{in}/q''_{CHF} > 1$. On the contrary, for $\xi_{in} \leq 10^3$, the stable area is smaller, restrained to the region near the $N_{sub} = N_{pch}$ line. However the flowrate is larger at smaller $\xi_{in} \leq 10^3$.

These observations are in agreement with the marginal stability predictions as a function of ξ_{in} (Figure 7b). Differences with the analytical model are likely due to the homogeneous flows model assumption from [17], which differs from the numerical CATHARE flow model. In addition, the apparition of instabilities below in the DWO stable domain is due to other types of instabilities. They also agree with the present experimental and numerical observations, where the upstream pressure loss was seen to stabilize the flow.

6. Conclusion

Experiments and simulations with the system-scale code CATHARE of natural circulation at P_{atm} were carried out with various singular pressure losses in the hot leg (HL) and cold leg (CL) respectively downstream and upstream the test-section. At low power, the flow is stationary and stable, while flow reversals are observed at larger input power. The boundary between these regimes strongly depends on the downstream pressure loss coefficients.

First the CATHARE code is able to properly simulate the configuration of a natural circulation loop operating close to atmospheric pressure. In the stable regime, CATHARE simulations are in good agreement with the experimental results. The flowrate, the mixture temperature and pressure drop over the test-section are similar. Moreover, the stability boundaries are close, and given by straight lines in the (q''_{in}, N_{sub})-plane. In the flow reversal regime, similar reversal frequencies are observed in the numerical simulations and in the experiment.

In addition, the stability criterion from Guanghi et al. [17] is verified both in experiments and simulations, by considering the equivalent pressure loss coefficients of the CL and HL. The experimental results presented here confirm previous studies on flow instabilities, i.e. [4, 10–12, 21, 24, 36]. The numerical results assess the ability of system-scale codes to reproduce the phenomenon.

For the EXOCET design, the DWO unstable triangle is bounded by $N_{sub,max} \approx 300$, $x_{out} = 0$ (i.e. the CHF) and line C. This zone can be reduced by increasing ξ_{in}. In these cases, stable boiling configurations are observed numerically, $x_{out} > 0$. This allows to benefit from cooling thanks to the water latent heat.

The flowrate deviation between experiments and simulations is around 10%. This could potentially be reduced by focusing on modelling of physical phenomena at low pressure. The results presented here participate in extending the code validity domain.

Stability boundaries have to be taken into account for the design. Indeed, boiling is a very efficient way to remove heat in a system. The increase in upstream pressure loss increases the stability region to large void fractions. The flowrate would decrease, but the efficiency of the heat removal would benefit from the latent heat. Moreover, the driving force would increase due to boiling, and would counterbalance the effect of the upstream pressure loss. The thermomechanical behavior of the exchangers in the unstable regime could be characterized and studied. Indeed, the exchangers could be used in this configuration.

Acknowledgment

Authors acknowledge fruitful discussions with Jean-Philippe Descamps, Fabrice François, Philippe Dufeil, Antoine Gerschenfeld, Sylvain Vitry and Eric Hanus.

CRediT author statement

SRdV: Investigation; Formal Analysis; Visualization; Writing - initial draft, review & editing. **PA:** Investigation; Writing - review & editing. **BG:** Conceptualization; Software development; Writing - review & editing. **LR:** Conceptualization; Writing - review & editing.

References

[1] P. K. Vijayan, A. K. Nayak, N. Kumar, Single-phase, Two-phase and Supercritical Natural Circulation Systems, Woodhead Publishing, 2019.

[2] J. Bouré, A. Bergles, L. Tong, Review of two-phase flow instability, Nuclear engineering and design 25 (2) (1973) 165–192.

[3] V. Jain, A. Nayak, P. Vijayan, D. Saha, R. Sinha, Experimental investigation on the flow instability behavior of a multi-channel boiling natural circulation loop at low-pressures, Experimental Thermal and Fluid Science 34 (6) (2010) 776–787.

[4] X. Chen, P. Gao, S. Tan, Z. Yu, C. Chen, An experimental investigation of flow boiling instability in a natural circulation loop, International Journal of Heat and Mass Transfer 117 (2018) 1125–1134.

[5] S. Y. Lee, D. W. Lee, Linear analysis of flow instabilities in an open two-phase natural circulation loop, Nuclear Engineering and Design 128 (3) (1991) 317–330.

[6] Y. Lin, C. Pan, Non-linear analysis for a natural circulation boiling channel, Nuclear Engineering and Design 152 (1-3) (1994) 349–360.

[7] H. Jeng, P. Chin, Multiple steady state solutions for a two-phase natural circulation loop with subcooled boiling, in: Proceedings of the fourth international topical meeting on nuclear thermal hydraulics, operations and safety. Vol. 1, 1994.

[8] C. Wu, S. Wang, C. Pan, Chaotic oscillations in a low pressure two phase natural circulation loop under low power and high inlet subcooling conditions, Nuclear engineering and design 162 (2-3) (1996) 223–232.

[9] S. Wang, J. Wu, P. Chin, W. Lin, Thermal-hydraulic oscillations in a low pressure two-phase natural circulation loop at low powers and high inlet subcoolings, in: 4th International Topical Meeting on Nuclear Thermal Hydraulics, Operations and Safety, 2004.

[10] M. Ishii, Thermally induced flow instabilities in two-phase mixtures in thermal equilibrium, Georgia Institute of Technology, 1971.

[11] S. Shi, Y. Lin, W. Yang, M. Ishii, Experimental stability maps for a BWR-type small modular reactor, in: Proceedings of the 16th International Topical Meeting on Nuclear Reactor Thermal Hydraulics (NURETH-16), Chicago, IL, 2015.

[12] S. Shi, J. P. Schlegel, C. S. Brooks, Y.-C. Lin, J. Eoh, Z. Liu, Q. Zhu, Y. Liu, T. Hibiki, M. Ishii, Experimental investigation of natural circulation instability in a BWR-type small modular reactor, Progress in nuclear energy 85 (2015) 96–107.

[13] Y. Kozmenkov, U. Rohde, A. Manera, Validation of the relap5 code for the modeling of flashing-induced instabilities under natural-circulation conditions using experimental data from the circus test facility, Nuclear Engineering and Design 243 (2012) 168–175.

[14] C. Tompkins, M. Corradini, Flow pattern transition instabilities in a natural circulation cooling facility, Nuclear Engineering and Design 332 (2018) 267–278.

[15] K. Fukuda, T. Kobori, Classification of two-phase flow instability by density wave oscillation model, Journal of Nuclear science and Technology 16 (2) (1979) 95–108.

[16] U. Rohatgi, R. Duffey, Stability, DNB, and CHF in natural circulation two-phase flow, International communications in heat and mass transfer 25 (2) (1998) 161–174.

[17] S. Guanghui, J. Dounan, K. Fukuda, G. Yujun, Theoretical and experimental study on density wave oscillation of two-phase natural circulation of low equilibrium quality, Nuclear Engineering and Design 215 (3) (2002) 187–198.

[18] L. E. O'Neill, I. Mudawar, Review of two-phase flow instabilities in macro-and micro-channel systems, International Journal of Heat and Mass Transfer 157 (2020) 119738.

[19] D. Brutin, F. Topin, L. Tadrist, Experimental study of unsteady convective boiling in heated minichannels, International journal of heat and mass transfer 46 (16) (2003) 2957–2965.

[20] R. Jones, R. Judd, An investigation of dryout/rewetting in subcooled two-phase flow boiling, International journal of heat and mass transfer 46 (17) (2003) 3143–3152.

[21] Z. Li, P. Gao, Y. Lin, Y. Zhang, P. Ji, C. Zou, Investigation on flow instability in a natural circulation loop with rod bundles, Annals of Nuclear Energy 132 (2019) 212–226.

[22] D. D. Hall, I. Mudawar, Critical heat flux (chf) for water flow in tubes—i. compilation and assessment of world chf data, International Journal of Heat and Mass Transfer 43 (14) (2000) 2573–2604.

[23] D. D. Hall, I. Mudawar, Critical heat flux (CHF) for water flow in tubes—II.: Subcooled CHF correlations, International Journal of Heat and Mass Transfer 43 (14) (2000) 2605–2640.

[24] Z. Guozhi, C. Xinrong, S. Xingwei, A study using RELAP5 on capability and instability of two-phase natural circulation flow under passive external reactor vessel cooling, Annals of Nuclear Energy 60 (2013) 115–126.

[25] Q. Wang, P. Gao, X. Chen, Z. Wang, Y. Huang, An investigation on flashing-induced natural circulation instabilities based on RELAP5 code, Annals of Nuclear Energy 121 (2018) 210–222.

[26] N. Alpy, M. Anderhuber, A. Gerschenfeld, J. Perez-Manes, E. Bissen, C. Latge, M. Medale, Some numerical achievements on Na boiling dynamics and next technical route, Nuclear Engineering and Design 365 (2020) 110728.

[27] S. Renaudière de Vaux, B. Grosjean, Effect of upstream and downstream pressure losses on flow reversals in low-pressure natural circulation loops, in: Proceedings of the ATH 2022 meeting, Anaheim, California.

[28] F. Barre, M. Bernard, The CATHARE code strategy and assessment, Nuclear engineering and design 124 (3) (1990) 257–284.

[29] D. Bestion, The physical closure laws in the CATHARE code, Nuclear Engineering and design 124 (3) (1990) 229–245.

[30] P. Emonot, A. Souyri, J. Gandrille, F. Barré, CATHARE-3: A new system code for thermal-hydraulics in the context of the NEPTUNE project, Nuclear Engineering and Design 241 (11) (2011) 4476–4481.

[31] CEA, Website of the CATHARE code.
URL `https://cathare.cea.fr/`

[32] M. Ishii, T. Hibiki, Thermo-fluid dynamics of two-phase flow, Springer Science & Business Media, 2010.

[33] I. Idel'Cik, M. Meury, Memento des pertes de charge: coefficients de pertes de charge singulières et de pertes de charge par frottement, Eyrolles Paris, 1986.

[34] H. Blasius, Das aehnlichkeitsgesetz bei reibungsvorgängen in

flüssigkeiten, in: Mitteilungen über Forschungsarbeiten auf dem Gebiete des Ingenieurwesens, Springer, 1913, pp. 1–41.

[35] D. Groeneveld, J. Shan, A. Vasić, L. Leung, A. Durmayaz, J. Yang, S. Cheng, A. Tanase, The 2006 CHF look-up table, Nuclear engineering and design 237 (15-17) (2007) 1909–1922.

[36] S. Shi, T. Hibiki, M. Ishii, Startup instability in natural circulation driven nuclear reactors, Progress in Nuclear Energy 90 (2016) 140–150.

[37] M. Ishii, Investigation of natural circulation instability and transients in passively safe small modular reactors, Tech. rep., Purdue Univ., West Lafayette, IN (United States) (2016).

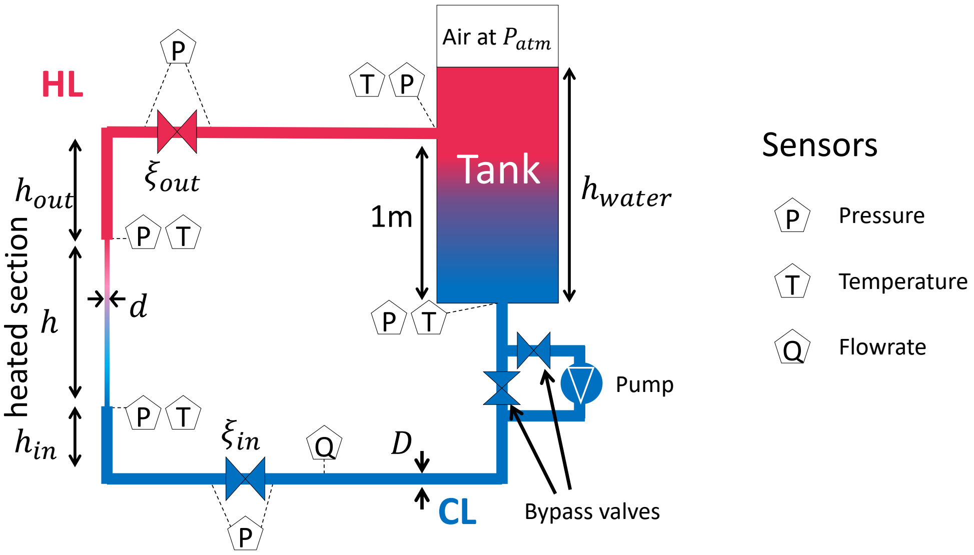

Figure 1: Sketch of the EXOCET facility showing the regulation valves and the pump used for loop characterization. Not to scale.

h	h_{out}	h_{in}	h_{water}	D	d	ξ_{in}, ξ_{out}	L_{CL}	L_{HL}
2.7 m	0.65 m	1.0 m	2.0 m	0.1 m	0.02 m	1 to 10^6	8.35 m	5.0 m

Table 1: Geometric properties of the EXOCET loop.

Parameter	Range
P	$P_{atm} \approx 1$ bar
q''_{in}	0-250 kW/m^2
T_{in}	15-80°C

Table 2: Range of parameters for the EXOCET loop.

Sensor	Range	Uncertainty
Differential pressure	$[0; 2]$ bar	± 0.001 bar
Pressure	$[0; 2]$ bar	± 0.002 bar
Pt100	$[0; 200]$°C	± 0.1°C
Thermocouples	$[0; 200]$°C	± 1°C
Flowmeter	$[-0.2; 0.5]$ kg/s	± 0.002 kg/s

Table 3: Sensor types and associated uncertainties.

	a_0	a_1	a_2	a_3
ξ_{in}	7.194	-0.1267	1.121×10^{-3}	-3.809×10^{-6}
ξ_{out}	9.111	-0.2170	2.569×10^{-3}	-1.069×10^{-5}

Table 4: Values of the polynomial fitting functions coefficients.

	$\frac{\Delta T_{out}}{\Delta T_{sat}}$	G	ΔP_{TS}	ΔP_{CL}	ΔP_{HL}
MAE	5.68%	9.31%	8.86%	10.66%	105%
ME	-0.36%	9.19%	-8.86%	10.66%	-97%
RMS	6.44%	11.71%	8.90%	10.70%	120%

Table 5: Values of error indicators for the mass velocity G, $\frac{\Delta T_{out}}{\Delta T_{sat}}$, and the pressure losses.

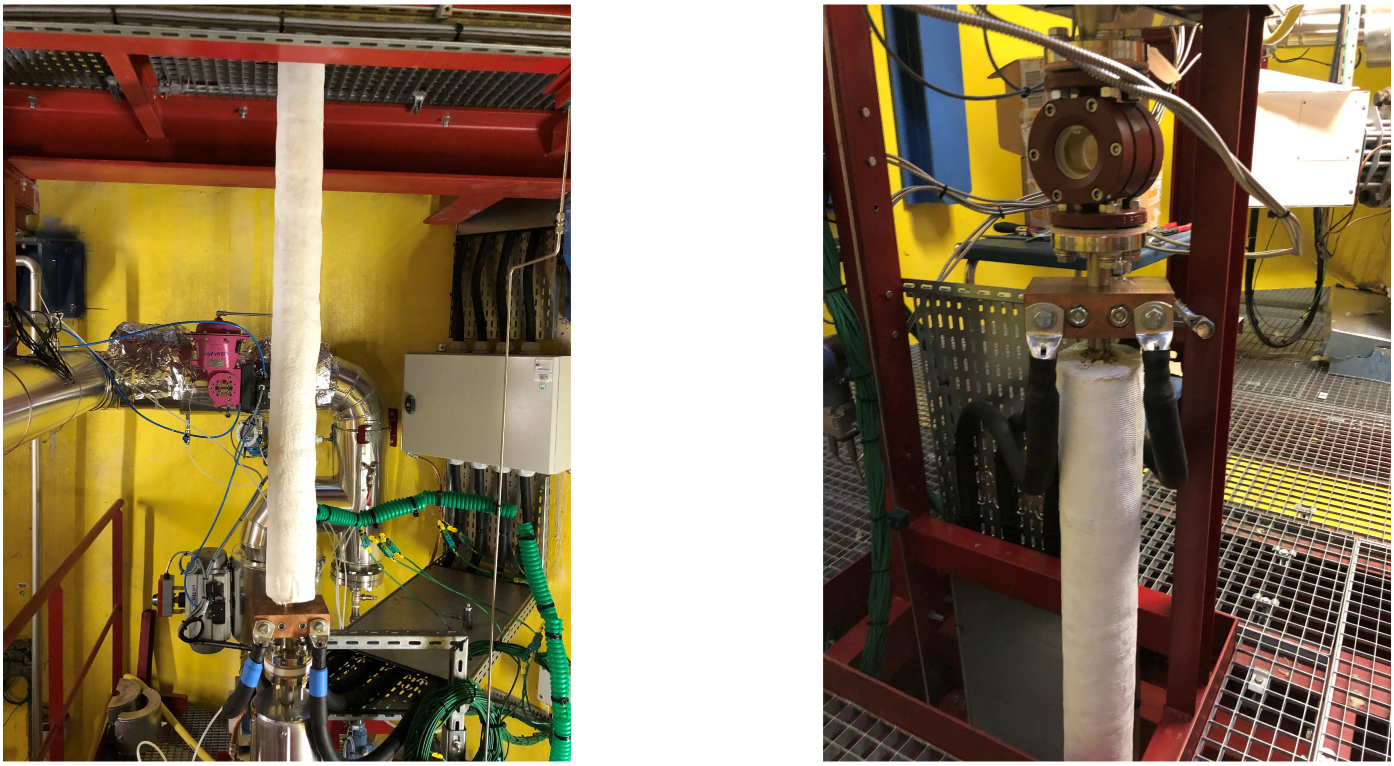

(a) Inlet of the test-section.

(b) Outlet of the test-section and visualization window.

Figure 2: Photos of EXOCET test-section, showing the insulation and the visualization window.

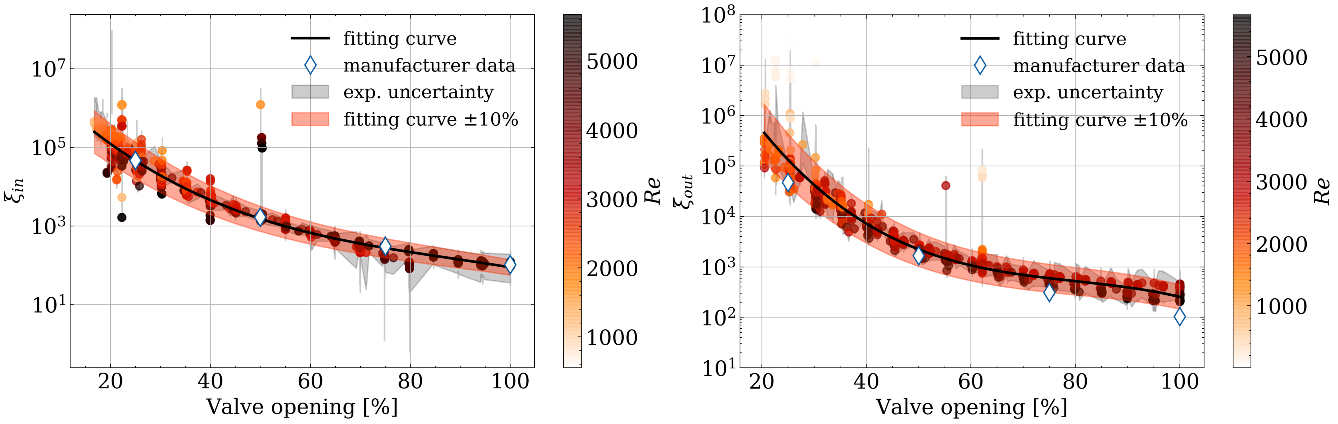

(a)

(b)

Figure 3: Singular pressure loss coefficients measured with imposed flow. Symbols are instantaneous measurements colored by Re. The black line is a 3rd order polynomial fit of $\log_{10}(\xi_{in})$ and $\log_{10}(\xi_{out})$. The grey area shows ±10% interval on the polynomial coefficients values.

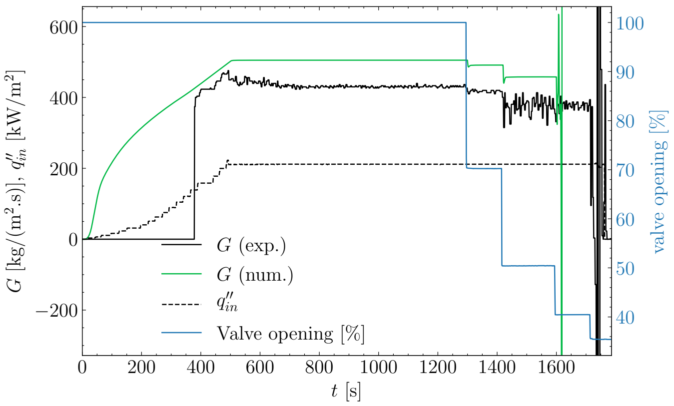

Figure 4: Example of time evolution of downstream valve opening (right scale), mass flux G and imposed power q''_{in} (left scale), experimental and numerical data.

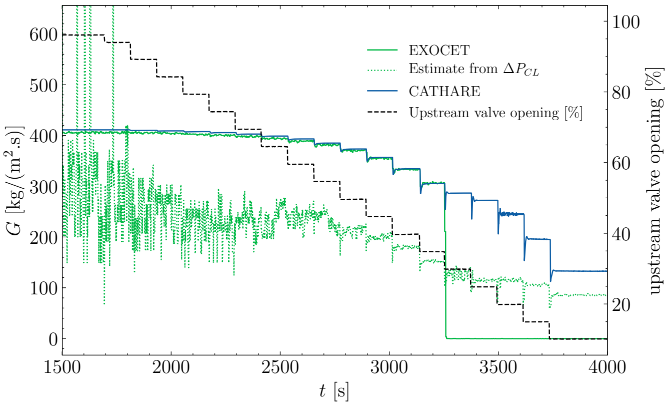

Figure 5: Example of time evolution of upstream valve opening (right scale), mass flux G (left scale), Here q''_{in} = 135 kW/m^2, experimental and numerical data.

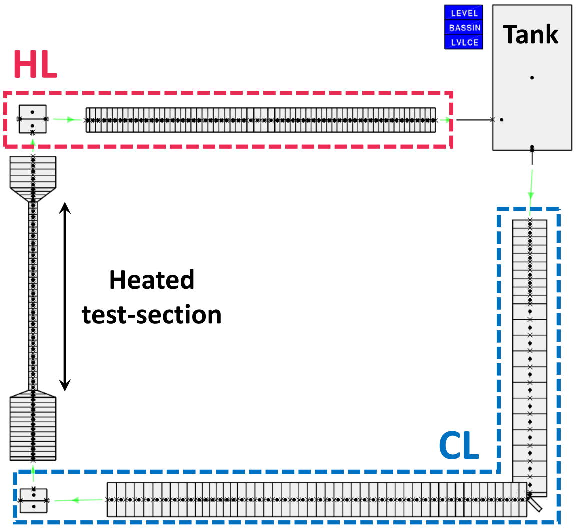

Figure 6: View of the EXOCET numerical model and mesh with the graphical user interface GUITHARE of CATHARE.

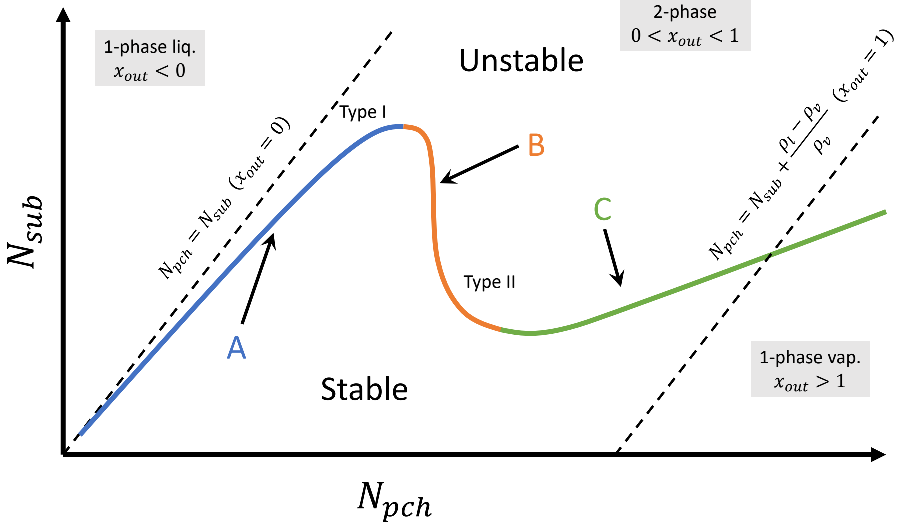

(a) Typical shape of the marginal stability boundary.

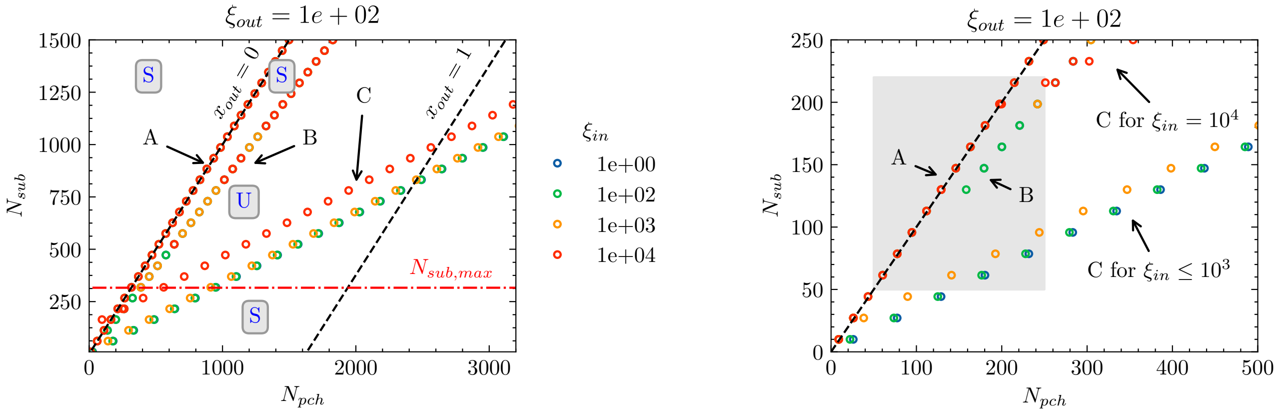

(b) Marginal stability lines in the EXOCET configuration based on the criterion of [17].

(c) Same graph zoomed to area of interest for EXOCET, shaded in grey.

Figure 7: Natural circulation stability curves. Stable and unstable zones are labelled S and U in the left figure.

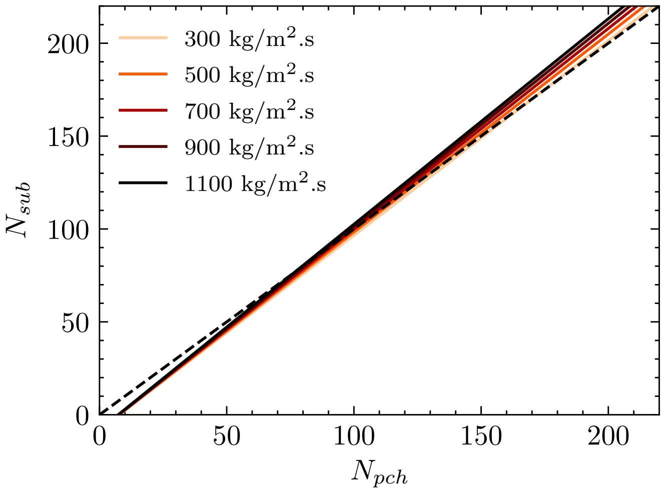

Figure 8: N_{pch}^{CHF} computed from (16) as a function of N_{sub} and G.

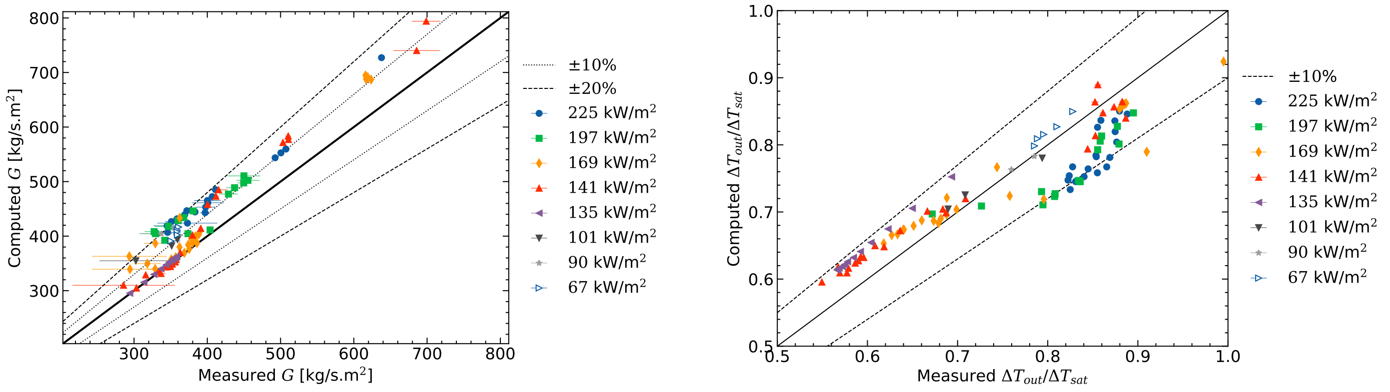

(a) (b)

Figure 9: Comparison of numerical and experimental results in the stable regime for the mass flux G and the ΔT_{out}. The horizontal error bars represent the RMS of the temporal fluctuations for G; and the experimental uncertainty for $\Delta T_{out}/\Delta T_{sat}$ (see Table 3).

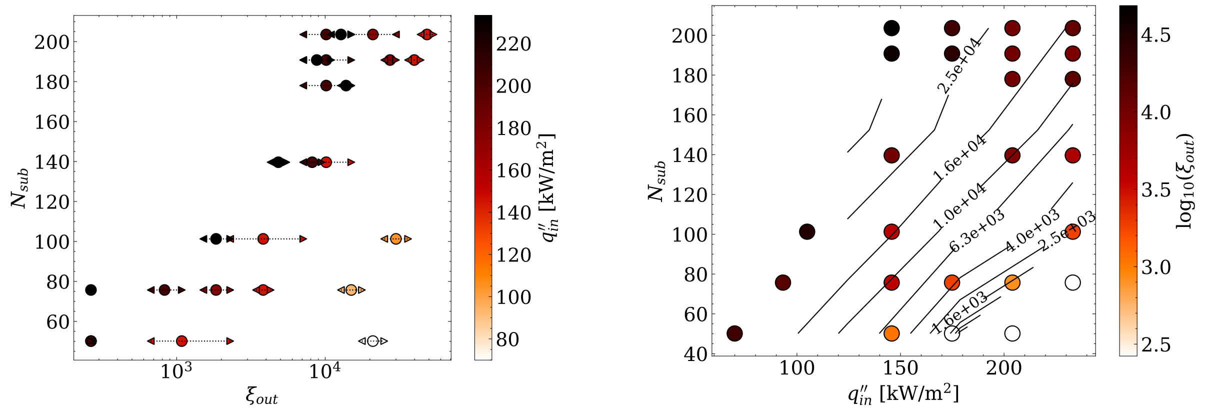

(a) (b)

Figure 10: Experimental phase diagram as a function of the downstream valve pressure loss coefficient ξ_{out} and the wall heat flux q''_{in}. Data shown in (a) the (ξ_{out}, N_{sub})-plane and in (b) the (q''_{in}, N_{sub})-plane. In (a), the ◄ and ► symbols represent the ξ_{out} values before and after the flow reversals, respectively. The • symbols represent the ξ_{out} value of the average between the valve opening X_{out} before and after the apparition of flow reversal. In (b), the lines are interpolated stability boundaries.

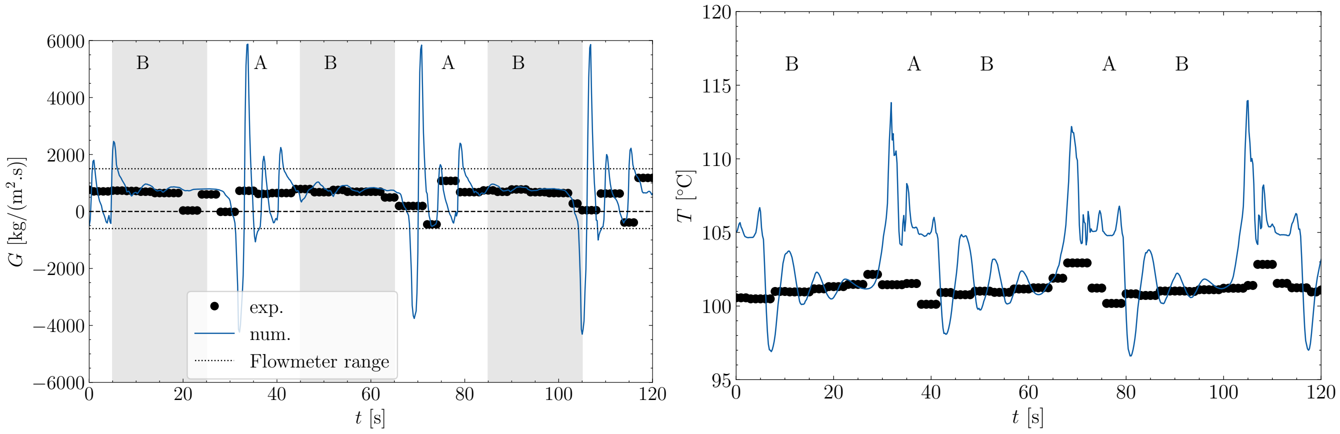

(a) Flowrate.

(b) Temperature at test-section exit.

Figure 11: Time-evolution in the reversal regime. Black: experiment; blue: numerical simulation. The experiment was carried out at $q''_{in} = 206$ kW/m^2, $T_{in} = 70$°C. In the simulation the pressure losses were fixed at $\xi_{in} = \xi_{out} = 10^3$. In the experiment the upstream valve was fully open and the downstream valve was 60% open.

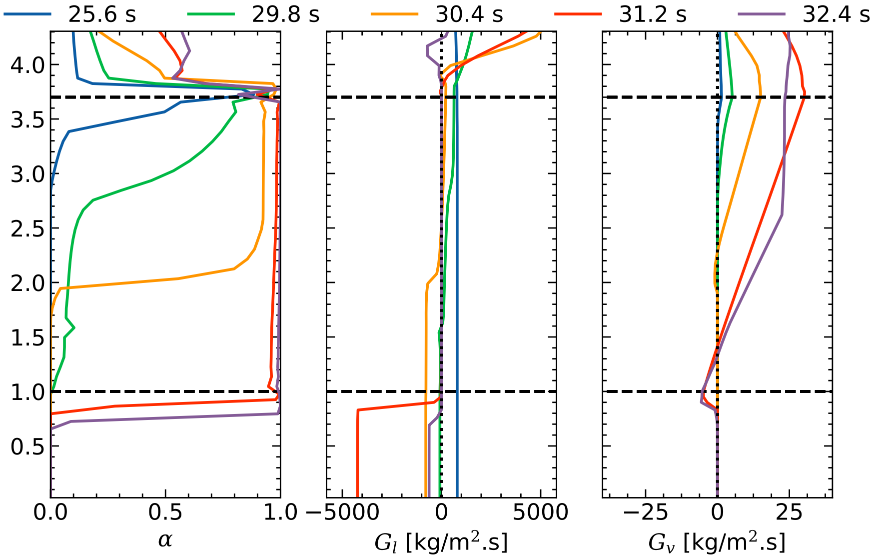

Figure 12: Profiles of void fraction α, liquid mass flux G_l and vapor mass flux G_v at five different instants during the first oscillation. The horizontal dashes show the beginning and end of the heated portion. The supplementary video shows several cycles.

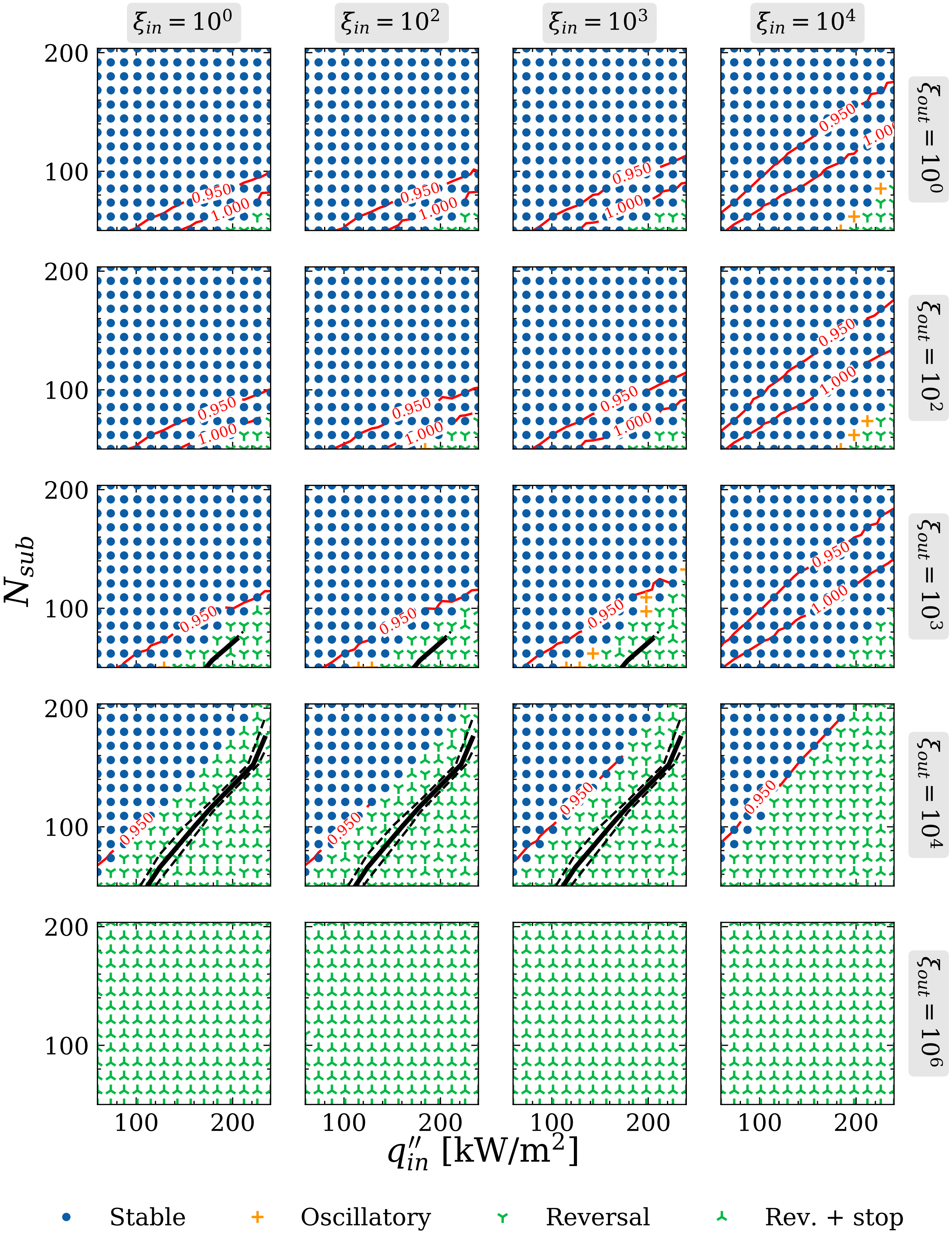

Figure 13: Numerical phase diagram in the (q''_{in}, N_{sub})-plane. Experimental boundaries are given by the black lines. Solid line: $\xi_{out} = 10^3$ (third row), $\xi_{out} = 10^4$ (fourth row). The dashed lines are the experimental boundaries, determined using the values of the valve opening before and after the apparition of flow reversal. The red lines show iso-values of $q''_{in}/q''_{CHF} = [0.95, 1.0]$, computed from equation (15).

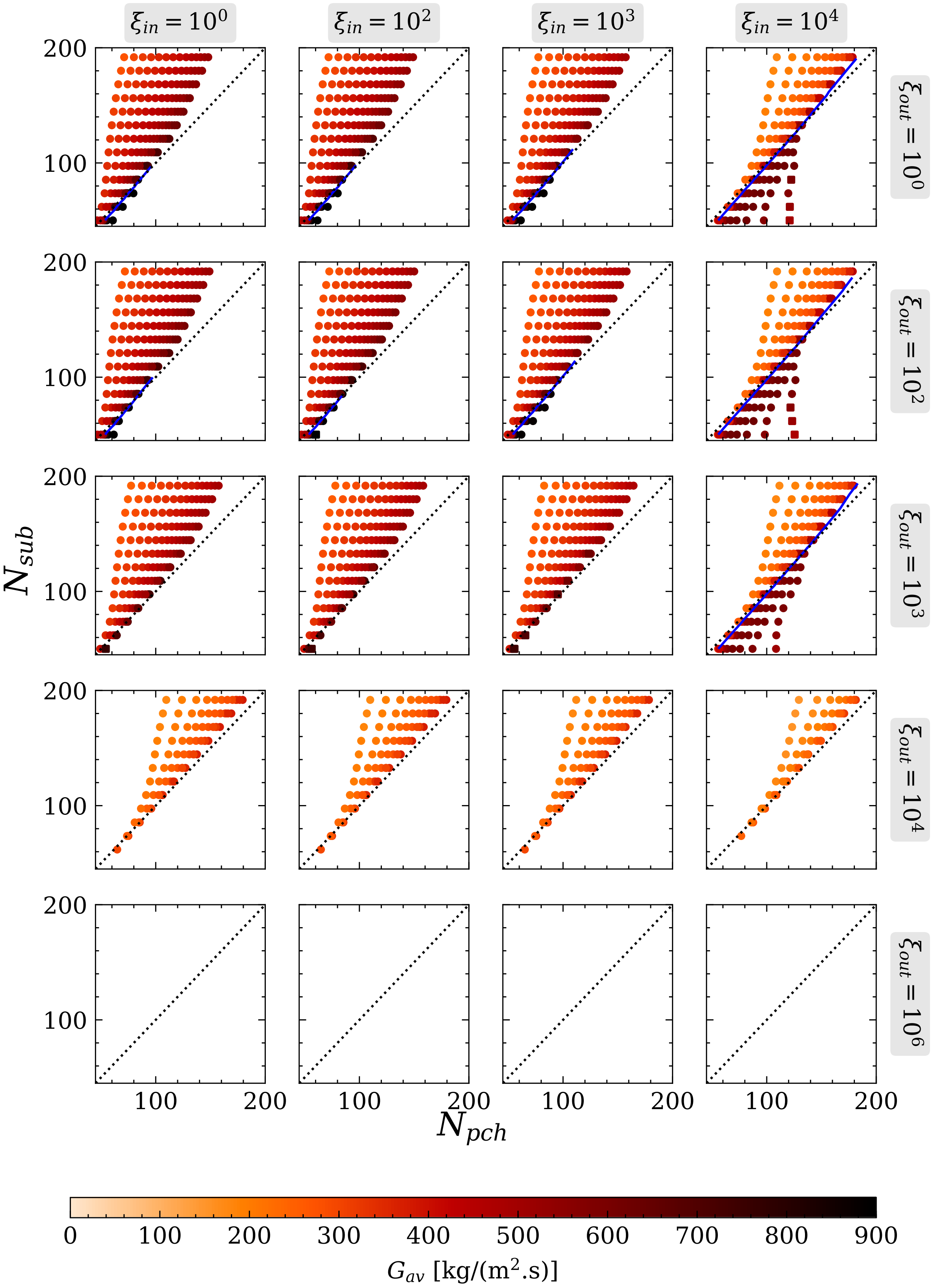

Figure 14: Numerical phase diagram in the (N_{pch}, N_{sub})-plane, colored by the average mass flux G_{av}. Circles: stable regime. Squares: oscillatory regime. Dotted black line: boiling line $N_{pch} = N_{sub}$. Solid blue line: CHF curve from equation (16).